1D GEOMECHANICAL MODELING AND CRITICALLY-STRESSED FRACTURES ANALYSIS IN NATURALLY FRACTURED RESERVOIR, MUARA LABOH GEOTHERMAL FIELD, WEST SUMATRA, INDONESIA

Taufik Al Amin[1], Marino Christiano Baroek[2], Sonny Santana[2], Benyamin Sapiie[1], Indra Gunawan[1]

1. Geological Engineering Study Program, Faculty of Earth Science and Technology, Institut Teknologi Bandung (ITB), Jl. Ganesha No.10, Bandung, Jawa Barat, Indonesia.
    Email: 22020309@mahasiswa.itb.ac.id
2. Supreme Energy, Menara Sentraya, Jl. Iskandarsyah Raya No.1A, RT.3/RW.1, Melawai, Jakarta Selatan, Jakarta.

Sari – Efektivitas struktur geologi untuk membantu aliran fluida dipengaruhi oleh faktor bentuk geometri struktur geologi tersebut dan tegasan lokal. Beberapa investigasi telah menunjukkan bahwa rekahan/sesar kritis *(critically stressed fractures)* menyebabkan dilatasi dan pergeseran pada bidang rekahan dan dapat menjadi zona permeabel. Analisis geomekanika satu dimensi (1D) dan rekahan kritis dilakukan di salah satu sumur pengembangan ML-2, di lapangan geotermal Muara Laboh, Sumatra Barat, Indonesia. Tujuan utama dari penelitian ini adalah untuk menentukan pola permeabilitas pada rekahan/sesar dan hubungannya dengan tegasan in-situ saat ini.

Analisis ini menggunakan data sumur yang terdiri dari log tali kawat gambar, sinar gamma (GR), sonik, survei tekanan dan suhu, dan data pengeboran. Pemodelan geomekanik menerapkan estimasi nilai tegasan secara empiris menggunakan data log dan hasil uji tekanan, yang dikalibrasi dengan menggunakan *stress polygon* dan fenomena kemunculan tanda-tanda *borehole failure*. Analisis Mohr-Coulomb dan kriteria kegagalan digunakan untuk menentukan rekahan kritis. Hasil model geomekanika 1D menunjukkan bahwa rezim tegasan in-situ di sumur ML-2 didominasi oleh *strike-slip* dan arah tegasan horizontal maksimum sekitar N60°E, mengikuti arah tegasan medan jauh. Rekahan kritis lebih mungkin terjadi pada arah NNE-SSW dan kebalikannya. Intensitas tinggi rekahan kritis cenderung berhubungan dengan interval produktif/*feed zone*s.

Kata kunci: Analisis geomekanika, tegasan in-situ, rekahan kritis, permeabilitas, Muara Laboh.

Abstract – *The effectiveness of geological structures to promote fluid flow is influenced by both geometric factors of the structural context and the local stress field. Multiple investigations have demonstrated that critically stressed fractures/faults promote dilatation and slip at permeable zones. One-dimensional (1D) geomechanics and critically-stressed fractures analyses are carried out in one of the development well, ML-2, in Muara Laboh geothermal field, West Sumatra, Indonesia. The main purpose of this study is to establish the permeability pattern on fractures/faults and its relationship to the present-day in-situ stress.*

The analyses utilize wellbore data consisting of borehole images, gamma-ray (GR), shear and compressional sonic logs, pressure and temperature survey, and drilling data. Geomechanical modeling applies empirical stress estimation to log data and pressure test results, which is calibrated by stress polygon and the occurrence of wellbore failures. Linearized Mohr-Coulomb failure envelopes and failure criteria are used to determine the critically-stressed fractures. The 1D geomechanics model result shows that the in-situ stress regime in ML-2 well predominantly is strike-slip and the maximum horizontal stress direction is about N60°E, following far-field field stress direction. Critically-stressed fractures are more likely to happen in the NNE-SSW direction and its reciprocal. The high intensity of critically-stressed fractures tends to be associated with productive interval/feed zones.

Keywords: Geomechanics analysis, in-situ stress, critically-stressed fractures, permeability, Muara Laboh.

1. INTRODUCTION

Muara Laboh geothermal field is located in Sumatra Island, approximately 135 km SE of the capital of Padang, West Sumatra Province. The field was put on an operation in 2019 after completing development drilling in 2018 and currently is generating 85 MW net of electricity. Muara Laboh field is associated with pull-apart basin generated due to movement of right lateral Great Sumatran Fault (GSF) segments. The permeability distribution characteristic is concentrated on faults/fractures (Muraoka et al., 2010) and contact intrusions (Stimac et al., 2019; Baroek et al., 2018). Baroek et al. (2018) studied the distribution of reservoir

permeability in Muara Laboh geothermal field through the formation and fracture characterization using borehole image logs, cuttings, cores, pressure and temperature survey. The study showed that the magnitude of well performance or permeability did not appear to be well correlated with the total number of effective fractures.

Hennings et al. (2012) did a geomechanics study in the fractured basement Suban Gas field and showed a good relationship between the number of critically-stressed fractures and wells' performance. Critically-stressed fracture in the fault damage zone controls the permeability of the subsurface reservoir (Hennings et al., 2012; Barton et al., 1995). The presence of critical fractures is controlled by the fracture position concerning the in-situ stress setting, pore pressures, and frictional constant of the subsurface rock. One-dimensional (1D) geomechanics and critically-stressed fractures analyses are carried out in one of the development well, ML-2, in Muara Laboh geothermal field, West Sumatra. The main purpose of this study is to establish the permeability pattern on fractures/faults and its relationship to the present-day in-situ stress.

2. GEOLOGIC BACKGROUND

The Muara Laboh Geothermal Field is located on the island of Sumatra, West Sumatra Province, Indonesia (**Figure 1**). The oblique subduction of the Indo-Australian Plate against the Eurasian Plate causes the formation of the Bukit Barisan mountains and transcurrent dextral strike-slip faults trending northwest-southeast (Great Sumatran Fault). Muara Laboh is located between two segments of the Great Sumatran Fault (GSF), Suliti (south) and Siulak (north) segment (**Figure 2**) (Baroek et al., 2018).

The geology of Muara Laboh field, shown in **Figures 2** and **3** below, has been described in detail by Stimac et al. (2019), Mussofan et al. (2018), and Rosidi et al. (1996). Structural data from field geology mapping, rosette diagrams of surface structures and open fracture trends from specific locations and borehole image logs indicate three dominant orientations of

fracturing in Muara Laboh: N-S (extension fracture), NW-SE (shear fracture) and lesser WNW-ESE, and NE-SW (shear fracture) (Baroek et al., 2018 and Mussofan et al., 2018).
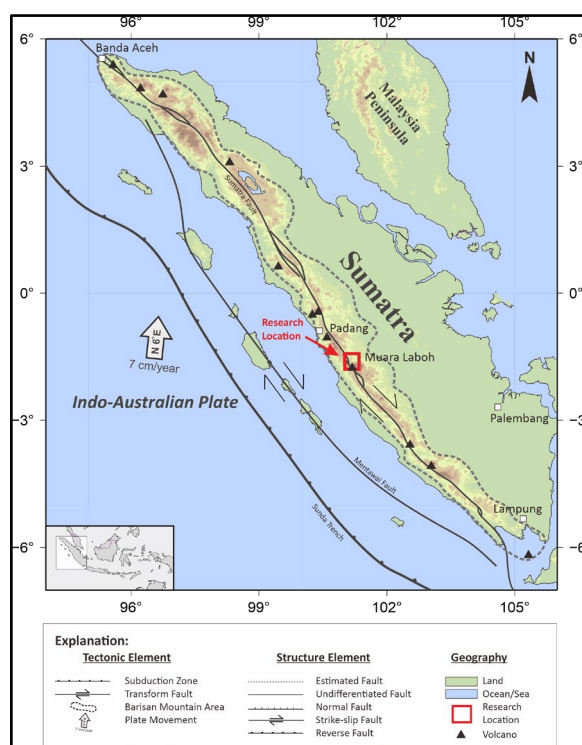

Figure 1. The tectonic setting of Sumatra Island and the Muara Laboh area mark with a red box on the map. Basemap based on CASMO.

The stratigraphy of Muara Laboh can be simplified into pre-Tertiary basement overlain by sequences of Tertiary to Mesozoic age volcanic, intrusions, and sediments (Mussofan et al., 2018). The oldest rocks in the Muara Laboh area comprise the Paleozoic Barisan Formation (Pb) consisting of slate, phyllite, hornfels, meta-greywacke, and limestone recrystallized to marble (Pbl). The Painan Formation (Tomp), consisting of mixed volcanic and sedimentary rocks, unconformably overlies the Pre-Tertiary basement. The volcanic sequence consists mainly of andesitic to dacitic lava, breccia, crystal tuff, ignimbrite, and lithic tuff. Undifferentiated Silicic Volcanic rocks (Qou and Qol) are widely distributed in the mountainous terrain northwest, west, and southwest of Muara Laboh field. These volcanic products consist of dacite, rhyodacite, rhyolite lava and tuff, crystal tuff, vitric tuff,
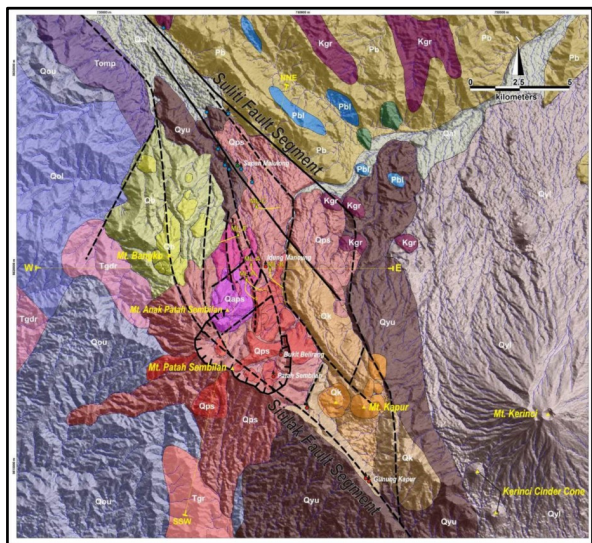
tuff-breccia, ignimbrite, and obsidian.

Figure 2. Geologic map of Muara Laboh area (Mussofan et al., 2018).
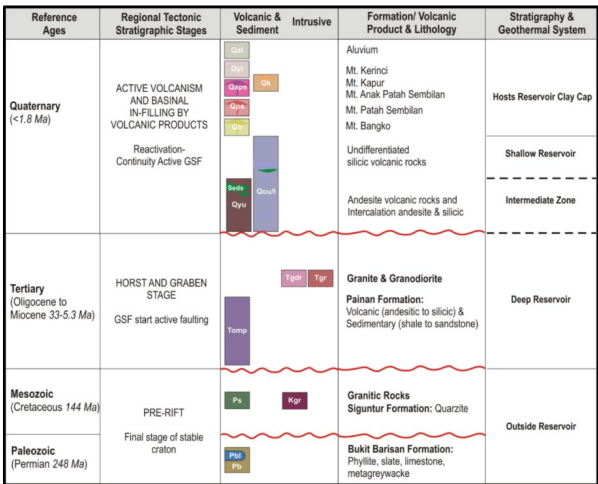

Figure 3. Simplified stratigraphy of Muara Laboh area (Mussofan et al., 2018).

The youngest sequence consists of Young Quaternary volcanic products that covered the earlier silicic and andesitic volcanic sequences over almost the entire Muara Laboh area. These products come from several eruption centers respectively from the NW to SE consist of Mt. Bangko, Mt. Patah Sembilan, Mt. Anak Patah Sembilan, Mt. Kapur, and Mt. Kerinci.

3. DATA AND METHODOLOGY
Data
The data used in this study came from the ML-2 primary data consisting of wireline log, pressure and temperature (PT) survey, and drilling data. The secondary data of petrophysics test results, surface geological map, internal reports regarding the updated structures and stratigraphy, and World Stress Map (WSM) were used in this study. Borehole images, gamma-ray (GR), and sonic logs were acquired at reservoir intervals. Meanwhile, pressure and temperature (PT) survey data cover the whole well intervals. Several sidewall core data in other Muara Laboh development wells whose petrophysical parameters have been analyzed are also used to complement the absence of data in ML-2 such as density logs. The completeness of the data can be seen in **Tables 1** and **2**.

Table 1. Data availability of ML-2.

Methodology
An example of a 1D geomechanics study is shown in **Figure 4** below, while the workflow of this study is summarized in **Figure 5**. One-dimensional (1D) geomechanics model consists of in-situ stress (magnitudes and orientations), pore pressures, formation elastic and strength properties, which were calibrated with formation pressure tests, the occurrence of wellbore failures, drilling data, and core test data upon availability. Pore pressure can be derived by direct measurement or estimated from a wireline log. Pore pressure in this study uses the direct measurement of the PT log.

Elastic properties, Young's modulus and Poisson's ratio are commonly used to describe the elastic properties and rock strength is represented by unconfined compressive strength (UCS), tensile strength (TS), and internal friction angle. The elastic properties and rock strength are derived from the rock

mechanic test. In the absence of rock mechanic test data, log-core correlation can be used to determine elastic properties and rock strength using sonic and density logs (**Table 3**).

There are in general three principal stresses that work on the earth's crust, one vertical (σ_v) and two horizontals: SHmax (σ_H) and Shmin (σ_h). The magnitude and orientation of these stresses vary and can be correlated with Anderson's fault classification (1951) of normal, strike-slip, or reverse faulting (Zoback, 2007). A normal fault stress regime shows that vertical stress is the maximum stress ($\sigma1$), where both horizontal stresses are the intermediate and least principal stresses ($\sigma2$ and $\sigma3$). Vertical stress becomes the intermediate stress in the strike-slip fault stress regime and the least principal stress in the reverse fault stress regime. Pore pressure estimation uses a direct measurement of the pressure-temperature shut-in survey that covers the whole wellbore intervals. The absence of density logs on the ML-2 well is replaced by making a polynomial regression using density data (**Table 2**) from the core plugs of other wells which would later be used to estimate vertical stress.

The image log data is evaluated for fractures interpretation and borehole failure features such as compressional and tensile failure (**Figure 6**). These features, integrated with estimations of rock strength, overburden stress, and mud fluid pressure, are used to estimate the maximum horizontal stress using the equation proposed by Barton et al. (1998). The minimum horizontal stress is obtained by estimation from the instantaneous shut-in pressure (ISIP) on extended leak-off tests (XLOT) data of the nearest well because of the absence of XLOT data on ML-2. Stress estimation using elastic and strength properties proposed by Higgins et al. (2008) as well as frictional strength based on frictional equilibrium theory proposed by Zoback and Healy (1992); Jaeger, (1979); Jaeger et al., (2007) is also used as shown in **Table 4**.

Horizontal stresses directions are determined utilizing image logs by evaluating borehole failures in the form of drilling-induced tensile fractures (DITF) and stress-induced wellbore breakouts. In vertical wells, the direction of SHmax is parallel with the direction of drilling-induced tensile fractures, meanwhile, the direction of Shmin is parallel with the direction of wellbore breakout (**Figure 6**). Breakouts directions in deviated holes vary significantly from what would occur in vertical holes (Zoback et al., 1985; Peska and Zoback, 1995), as well as drilling-induced tensile fractures. ML-2 is a deviated well and therefore horizontal stresses orientations need to be corrected using the equation proposed by Hiramatsu and Oka (1962, 1968) as cited in Fjær et al. (2008) with the stress transformation method is already explained in detail by Zoback et al. (2003).

Table 2. Petrophysical measurements on core plugs of several wells in Muara Laboh area. Data from Stimac et al. (2019).

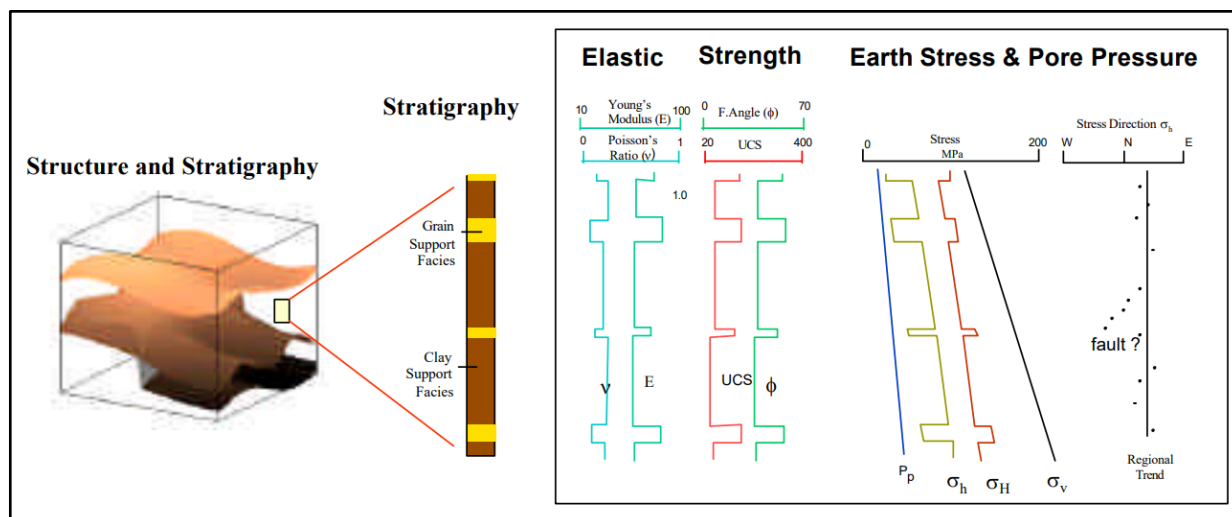| Well	Depth (mMD)	Vertical Depth (m)	Elev (masl)	Rock Type		Low pressure (see remarks)			Grain Density	Bulk Density	
						∅	K_{inf}	K_{air}			∅
						%	md	md	g/cm3	g/cm3	%
ML-H4	2581.82	2366.11	-796.35	Granodiorite	Intrusion	1.32	0.02	0.044	2.68	2.66	1.32
ML-H4	2585.67	2369.59	-799.83	Granodiorite	Intrusion	2.07	0.042	0.056	2.7	2.67	2.07
ML-H4	2588.15	2371.77	-802.01	Granodiorite	Intrusion	1.72	0.012	0.017	2.7	2.67	1.72
ML-H4	2588.65	2372.22	-802.46	Granodiorite	Intrusion	1.51	0.269	0.304	2.71	2.68	1.51
ML-H4	3100.6	2823.98	-1254.22	Diorite	Intrusion	0.99	0.3	0.331	2.73	2.72	0.99
ML-A2	710.3	686.92	744.35	Silicic andesite lava breccia	Lava breccia	6.87	0.464	0.544	2.76	2.63	6.87
ML-A2	711.5	687.88	743.39		Lava breccia	3.82	0.002	0.01	2.74	2.67	3.82
ML-A2	715.6	691.15	740.12		Lava breccia	4.01	0.008	0.014	2.72	2.65	4.01
ML-A2	717.4	692.58	738.69		Lava breccia	4.5	0.01	0.016	2.73	2.65	4.5
ML-A3	953.7	857.25	574.02	Rhyolite ash-floq tuff	Tuff	3.24	0.0005	0.0005	2.64	2.58	3.24
ML-A3	956.85	858.9	572.37		Tuff	4.42	0.299	0.437	2.67	2.59	4.42
ML-A3	958.71	860	571.27		Tuff	3.23	0.721	0.769	2.66	2.61	3.23
ML-A3	2000.15	1454.7	-23.43	Rhyolite tuff	Tuff	0.245	0.0005	0.0005	2.65	2.65	
ML-A1	1553.3	1299.93	-132.68	Andesite lava breccia	Lava breccia	2.6		0.008	2.74	2.69	2.6
ML-B1	2179.95	1797.85	389.05	Basaltic andesite lava	Lava	2.2		0.023	2.77	2.73	2.2
ML-E1	1075	936.47	927.07	Rhyolite tuff	Tuff	3.8		0.009	2.66	2.6	3.8

Figure 4. Example of 1D geomechanics model which consists of strength and elastic properties, stress and pore pressure profile referenced on stratigraphy unit (Richard et al., 2007).
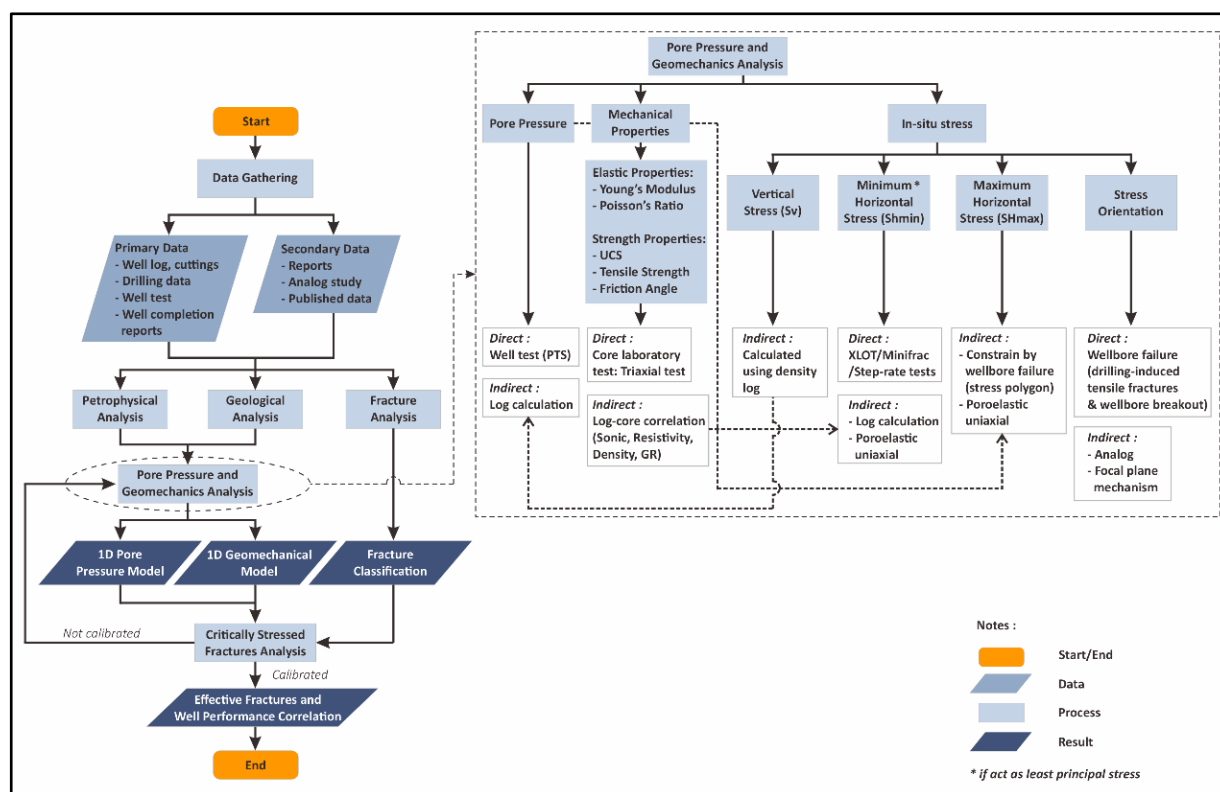

Figure 5. The workflows used in this research study.

Table 3. Empirical equations to calculate elastic and strength properties used in this research.

Mechanical Properties	Unit	Data Source	Empirical Equation	Notes
Poisson Ratio (v)	unitless	V_p and V_s derived from P-wave interval transit time (compressional sonic log)	$v = \dfrac{(V_p{}^2 - 2V_s{}^2)}{2(V_p{}^2 - V_s{}^2)}$	V_p and V_s correlation obtains by Greenberg and Castagna (1992) equation
Young's Modulus (E) - Dynamic	GPa	G and v derived from P- & S-wave interval transit time (compressional & shear sonic log).	$E = 2 \times G(1 + v)$	G obtain from $G = \rho \times V_s{}^2$
Young's Modulus (E) - Static	GPa	Δt_p or P-wave interval transit time (compressional sonic log), static young modulus would be firmly modelled if validation point from laboratory test available	$E = \left(0.076 \times \left(\dfrac{304.8}{\Delta t_p}\right)^{3.23}\right)$	Baroek (2016), unpublished
Unconfined Compressive Strength (UCS)	MPa	Δt_p or P-wave interval transit time (compressional sonic log)	$UCS = 129 + \left(\dfrac{4419.384}{\Delta t_p}\right)$	Zoback (2003)
Tensile Strength (T_0)	MPa	Unconfined Compressive Strength (UCS)	$T_0 = \dfrac{1}{10} \times UCS$	Perras and Diederichs (2014)
Internal Friction Angle (Φ)	degree	Porosity (ϕ) derived from P-wave interval transit time (compressional sonic log)	$\Phi = 57,8 - 105\phi$	Weingarten and Perkins (1995). Porosity is obtained by equation from Wyllie et al. (1958)

Table 4. Empirical equations to calculate stress parameters used in this research.

In-situ Stress Parameters	Data Source	Empirical Equation	Source
Pore Pressure (P_p)	PT Shut-in	-	-
Vertical Stress (S_v)	Density derived from P-wave interval transit time	$S_v = g \int_0^z \rho_b(z)\, dz$	Zoback (2007)
Minimum Horizontal Stress (S_{hmin})	S_v and P_p, validated using FIT & XLOT	$S_{hmin} = K_i(z)(S_v - P_p) + P_p$	Mathews and Kelly (1967)
Minimum Horizontal Stress (S_{hmin})	E, v, α, S_v and P_p	$S_{hmin} = \dfrac{v}{1-v}(S_v - \alpha P_p) + \alpha P_p + \dfrac{E}{1-v^2}\varepsilon_h + \dfrac{Ev}{1-v^2}\varepsilon_H$	Higgins et al. (2008)
Minimum and Maximum Principal Effective Stress	Friction constant	$\dfrac{\sigma_1}{\sigma_3} = \dfrac{S_1 - P_p}{S_3 - P_p} = \left[(\mu^2 + 1)^{1/2} + \mu\right]^2$	Jaeger and Cook (1979, 2007)
Maximum Horizontal Stress (S_{Hmax})	E, v, α, S_v and P_p	$S_{Hmax} = \dfrac{v}{1-v}(S_v - \alpha P_p) + \alpha P_p + \dfrac{E}{1-v^2}\varepsilon_H + \dfrac{Ev}{1-v^2}\varepsilon_h$	Higgins et al. (2008)

There are uncertainties in the calculation of the maximum horizontal stress, so it is necessary to validate the magnitudes that have been obtained. It is convenient to be able to simply estimate the range of possible stress states at any given depth and pore pressure given that stress in the crust is limited by the frictional strength of faults (Zoback, 2007). The frictional strength of the rock, which in this study employed a friction coefficient of 0.6 - 0.8 (Byerlee, 1978), limits the maximum horizontal stress magnitude, which is depicted as a polygon boundary. The existence of compressional and tensile failure manifested as wellbore breakout and drilling-induced tensile fractures in the borehole restrict the maximum permissible horizontal stress magnitude even further. Further explanation on how to utilize stress polygon and wellbore failure to constrain horizontal stress magnitude has been described in detail by Wiprut (2001) and Zoback (2007).

Fracture analyses were done utilizing image logs are also used for fracture analysis following the classification of Baroek et al. (2018). Baroek et al. (2018) divide fractures into conductive fracture (type 1), partially conductive fracture (type 2), and resistive fracture (type 3). There is one additional fracture, namely fractures associated with feed zones called effective fractures (type 4). In this study, only fractures of type 1, 2, and 4 are analyzed considering that type 3 fractures did not contribute to permeability because they are assumed to be filled with minerals and hence are impermeable. The open (type 1+2) and effective fractures (type 4) are examined in conjunction with the geomechanical model to determine critically-stressed fractures.
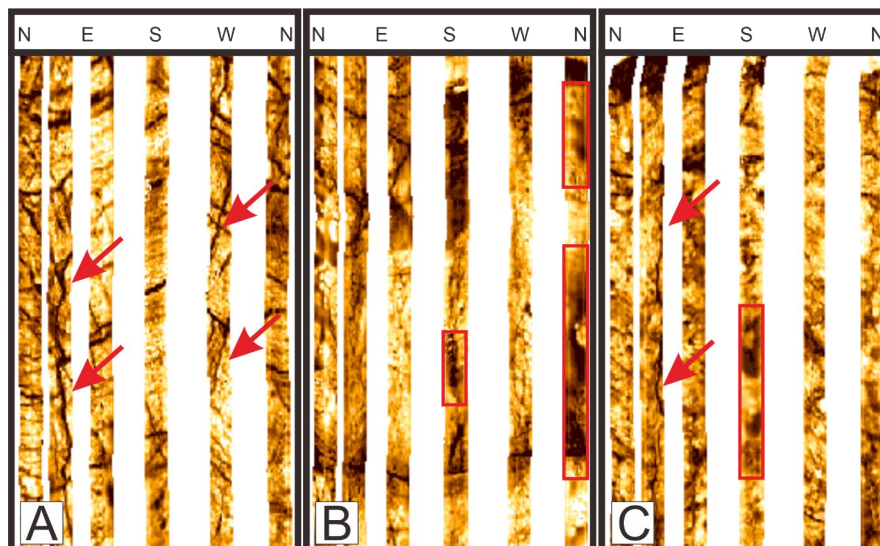
Figure 6. Image logs of ML-2 well with (A) drilling-induced tensile fractures, (B) wellbore breakout, and (C) both tensile fractures and breakouts in image logs. Wellbore breakouts appear as out-of-focus areas in electrical image data because of the poor contact of the electrode arrays on the pads of the tool where breakouts are present.
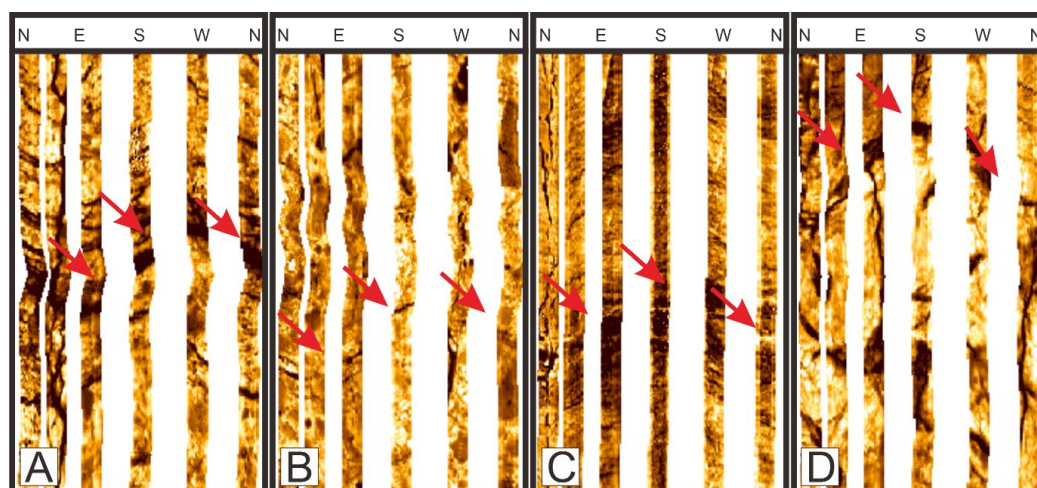

Figure 7. Examples of fractures found in ML-2, where the relative electrical resistivity of the wellbore wall is plotted from conductive (dark) to resistive (light). (A) Conductive fracture (type 1), (B) partial conductive fracture (type 2), (C) resistive fracture (type 3), and (D) conductive fracture associated with feed zone depth (type 4) marked with red arrows

The relationship between conductive fractures (type 1+2) and effective fractures (type 4) with the in-situ stresses is investigated further using geomechanical modeling. **Figure 8** shows a combined plot of fractures on the lower hemisphere projection contoured with Coulomb failure function (CFF) values, as well as projections of these fractures on a three-dimensional (3D) Mohr diagram to produce a critical fracture profile. Critical fractures can be recognized because the shear stress to normal stress ratio is more than 0.6 and the CFF value is greater than zero. Critically-stressed fractures are expected in the fractures domain that strikes north-south (N-S) to north northeast-south southwest (NNE-SSW) and its reciprocal, with a dip that is either vertical or sub-vertical. Other domain fractures have non-critical circumstances because each fracture plane has large normal stress and a small shear stress magnitude, resulting in shear stress to normal stress ratio of less than 0.6.
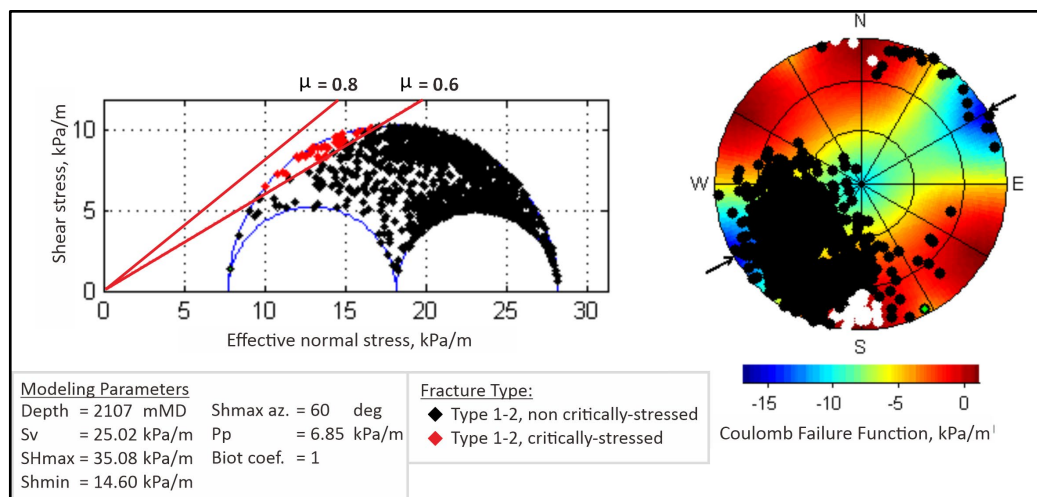
Figure 8. Fracture and stress summary illustrated with three-dimensional Mohr-Coulomb plots for frictional faulting (left). Critically-stressed fractures mark with a red diamond above coulomb failure envelope with 0.6 friction constant. Stereonets show plots of poles to the fracture types contoured for coulomb failure function (right).

4. RESULTS AND DISCUSSION
Mechanical Properties, In-Situ Stress, and Fractures

Figure 9 summarizes the geomechanics model of ML-2. To gain a complete picture of the rock-stress interaction, 1D geomechanics modeling with the characterization of the pore pressure profile and the three main stresses, overburden stress, horizontal maximum and minimum stresses, is supplemented by the calculation of rock mechanical properties. As shown in **Figure 9**, mechanical properties such as unconfined compressive strength (UCS) show the averaging value around 170-180 MPa which is included in very strong rock according to Attewell and Farmer, (1976) utilizing dynamic estimates with compressional and shear sonic as input calculation. The average friction angle of 55° also supports a competent rock type.

Tensile strength from empirical calculation utilizing the equation from Perras and Diederichs (2014) shows an average value of 17-18 MPa acceptable for volcanic rocks and fractured granites according to Lockner (1995).

Elastic parameters such as Young's modulus and Poisson's ratio reveal the rock's brittle nature, as seen by high values ranging from 3-9 GPa for static Young's modulus and 0.2-0.3 for Poisson's ratio.

In situ stress regime identified in well ML-2 reveals the strike-slip stress regime currently working in the Muara Laboh area. The principal stresses are validated by several direct drilling tests and the occurrence of wellbore failures of drilling-induced tensile fractures (DITF) and borehole breakouts. DITF interpreted from image log data in ML-2 is found to be abundant while breakout is more sparse. The sparse occurrence of breakouts is reasonable since the in-situ stress configuration around ML-2 is not large enough to compressively deform the surrounding rock formation that tends to be strong to very strong (180-200 MPa based on log estimation).
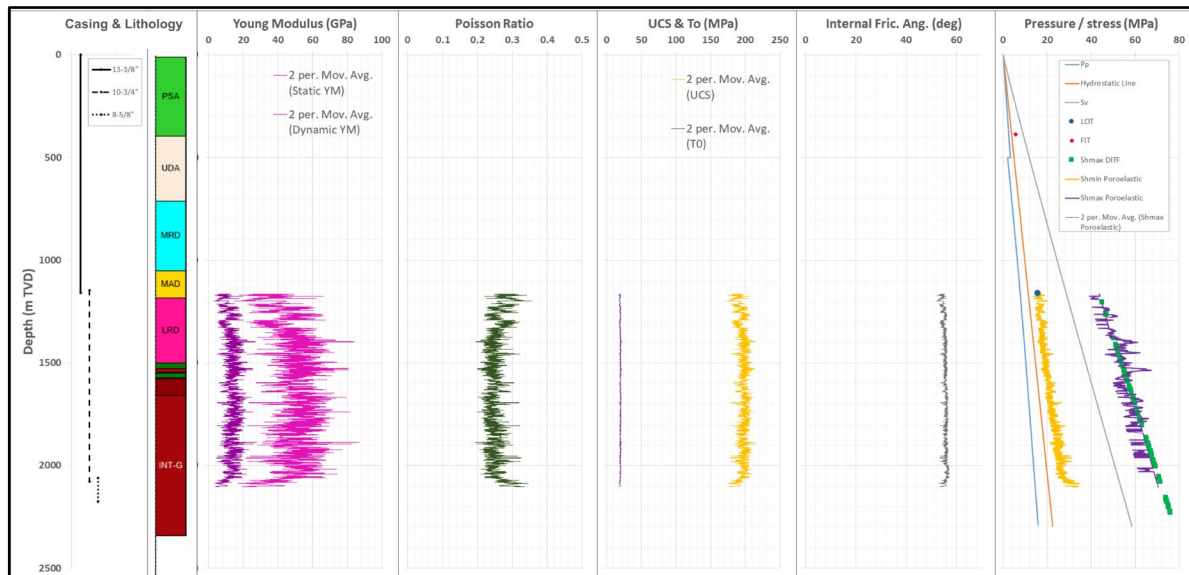
Figure 9. One-dimensional geomechanics model of ML-2.

Figure 10 shows another calibration of estimated horizontal stresses utilizing a stress polygon (Zoback, 2003). Stress polygon is derived by the frictional faulting theory (Jaeger and Cook, 1979), and by knowing the vertical stress and the pore pressure, both horizontal stress magnitude can be estimated. Horizontal stresses calculated were used and plotted in the stress polygon which is limited by the bottom boundary of the tensile failure line (blue color) and the border of the stress polygon using friction constants 0.6 and 0.8. Although the uncertainty of the friction value is an inevitability, a value of 0.6 - 0.8 is used in this study since the typical friction value in fractured granite is approximately 0.7. Even with a robust minimum horizontal stress magnitude estimation that has already been validated by the extended leak-off tests (XLOT), there is still a degree of uncertainty in maximum horizontal stress magnitude.

Wiprut (2001) explains that the steep slope of the blue tensile failure lines in **Figure 10** means a small uncertainty in the minimum horizontal stress creates a large uncertainty in the maximum horizontal stress. The maximum horizontal stress magnitude remains legitimate because a value below the tensile failure line is not feasible since observations in this depth indicate the presence of drilling-induced tensile fractures. Meanwhile, the maximum horizontal stress magnitude below the blue line indicates the absence of drilling-induced

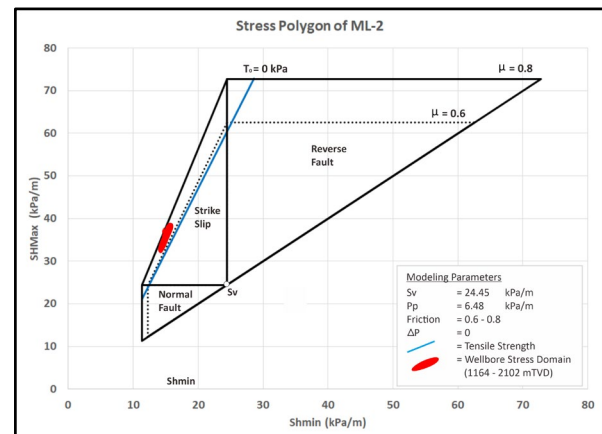tensile fractures (Wiprut, 2001).

Figure 10. Stress polygon (in gradient kPa/m) shows a strike-slip stress regime domain. Tensile failure for 0 kPa is indicated by the blue line. The red ellipse shows the results of the wellbore stress analysis. Model parameters are shown in the bottom right.

Drilling-induced tensile fractures in ML-2 are plotted on a rosette diagram and show a dominant frequency at N65°E and smaller values at N25°E (**Figure 11**). Since ML-2 is an inclined well-drilled azimuthally in the SW direction with an inclination up to 40°, hence drilling-induced tensile fractures identified from the image log need to be calibrated to remove the effect of borehole inclination and azimuth. This is done by evaluating the stress concentration around the wellbore wall.

Evaluation of stress concentration around the wellbore wall of ML-2 is carried out at 1810.5 mMD resulting in a lower stress concentration (shown in blue) around N60°E. The area with the largest stress concentration (shown in red) must be perpendicular to the area with the lowest stress concentration. This area of highest stress concentration is on an azimuth where the breakout is generally observed, however, no breakout is found in the required Co model. The lack of wellbore breakout is attributable to Muara Laboh's rock strength, which is quite high, as proven by UCS calculations utilizing wireline log data (**Figure 9).** This model demonstrates the consistency between the observations in the image log and the modeling performed.

Rock mechanics and elastic properties from ML-2 which shows strong, brittle, and stiff rock back up the preceding stress concentration around the wellbore wall model that showed the sparse occurrence of wellbore breakouts. Drilling-induced tensile fractures occur because the log data's rough estimation of tensile strength value in **Figure 9** displays a very low value compared to UCS around 15 MPa. Low-stress concentrations around the wellbore are very easy to develop tensile fractures because the general state of fractured rock is expected to be relatively low tensile strength (see Lockner, 1995).

A sufficiently high temperature of the wellbore environment will also weaken the rock, resulting in the easier occurrence of tensile fractures. The estimation of the maximum horizontal stress direction using the above modeling produces an azimuth direction of N60°E which generally follows the far-field stress in Sumatra (**Figure 12**). These findings are consistent with previous geomechanical analysis from Baroek et al. (2018) on three other wells in Muara Laboh, ML-D1, ML-H1, ML-H2, which shows the direction of maximum horizontal stress NE to ENE. Because of the inclined wellbore geometry, there is a 5° counterclockwise shift between the maximum horizontal stress direction from modeling and the drilling-induced tensile fractures direction observed in the image log. The 5° counterclockwise shift is due to the wellbore geometry drilled azimuthally subparallel to the direction of maximum horizontal stress resulting in a slight difference between the azimuth of drilling-induced tensile fractures and the azimuth of maximum horizontal stress.

The calculation of maximum horizontal stresses from logs utilizing the rock mechanical properties as input parameter shows quite a reasonable match with the calculation from wellbore failures implying that the maximum horizontal stress magnitude is well calibrated.

The previous in-situ stress investigation is very well suited to the regional tectonic context of West-Central Sumatra. In the back-arc area of Central Sumatra, Tingay et al. (2010) generate a general maximum horizontal stress trend using numerous wellbore and earthquake focal plane mechanisms data, resulting in NE-SW maximum horizontal stress direction. Muara Laboh reveals consistent findings which show maximum horizontal stress is about N60°E, matching with the data from World Stress Map (Heidbach et al., 2016, 2018) and Tingay et al. (2010). Since the ML-2 is wellbore drilled on a reservoir level depth, and the focal plane mechanism must be deeper, abundantly occurring on more than 10 km depth, the finding in this study is consistent. The strike-slip stress regime is likewise consistent when using earthquake focal plane mechanisms with a depth of 15-50 km and moment magnitude greater than 5, as indicated in the Global Centroid Moment Tensor (CMT) catalog data.
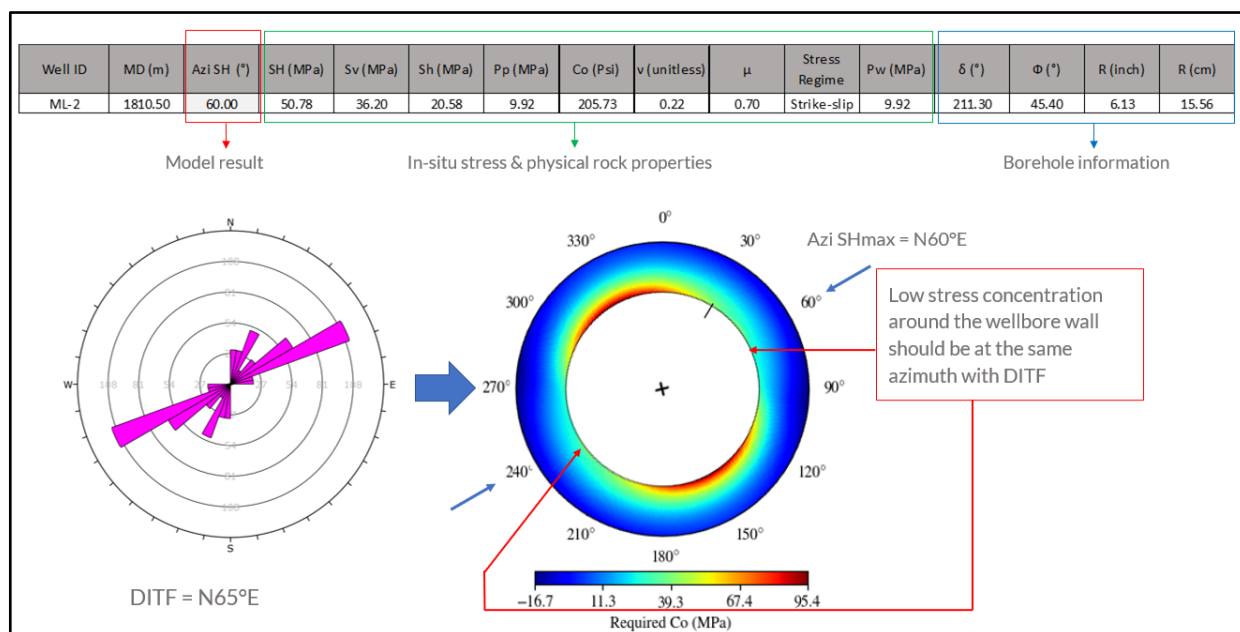
Well ID	MD (m)	Azi SH (°)	SH (MPa)	Sv (MPa)	Sh (MPa)	Pp (MPa)	Co (Psi)	v (unitless)	μ	Stress Regime	Pw (MPa)	δ (°)	Φ (°)	R (inch)	R (cm)
ML-2	1810.50	60.00	50.78	36.20	20.58	9.92	205.73	0.22	0.70	Strike-slip	9.92	211.30	45.40	6.13	15.56

Model result   In-situ stress & physical rock properties   Borehole information

Azi SHmax = N60°E

Low stress concentration around the wellbore wall should be at the same azimuth with DITF

DITF = N65°E

Required Co (MPa): −16.7   11.3   39.3   67.4   95.4

Figure 11. Stress concentration around wellbore modeling to interpret the azimuth of maximum horizontal stress. Drilling-induced tensile fracture (DITF) is interpreted from image log data. Note: azi SH = SHmax azimuth, Co = rock strength, μ = coefficient of internal friction, v = Poisson's ratio, δ = borehole azimuth and Φ = inclination.
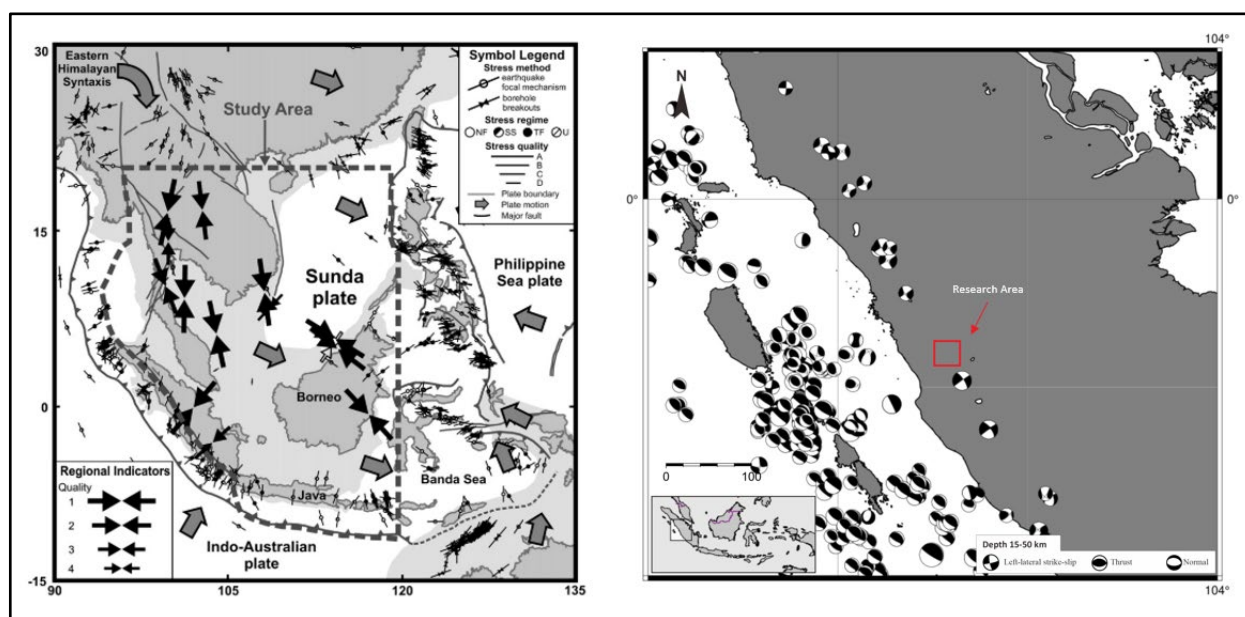
Figure 12. Maximum horizontal stress orientations within Southeast Asian stress provinces (left) and earthquake focal mechanism plot (right) in West-Central Sumatra. The research area is marked with a red rectangle. Data from World Stress Map (Tingay et al., 2010) and Global CMT Catalog (Dziewonski et al., 1981; Ekström et al., 2012).

Figure 13 shows a collection of detailed geological maps, regional structures, fracture types, and both maximum and minimum horizontal stress azimuths in the lower hemisphere projection. Maximum horizontal stress azimuth rotation occurs at various depths as evidenced by the rotation of wellbore failure features in the image logs. This rotation means that the setting of in-situ stresses is perturbed by the vicinity of active faults possibly because ML-2 is located in an active tectonic setting of an interpreted pull-apart basin due to the movement of Great Sumatran Fault (GSF) segments.
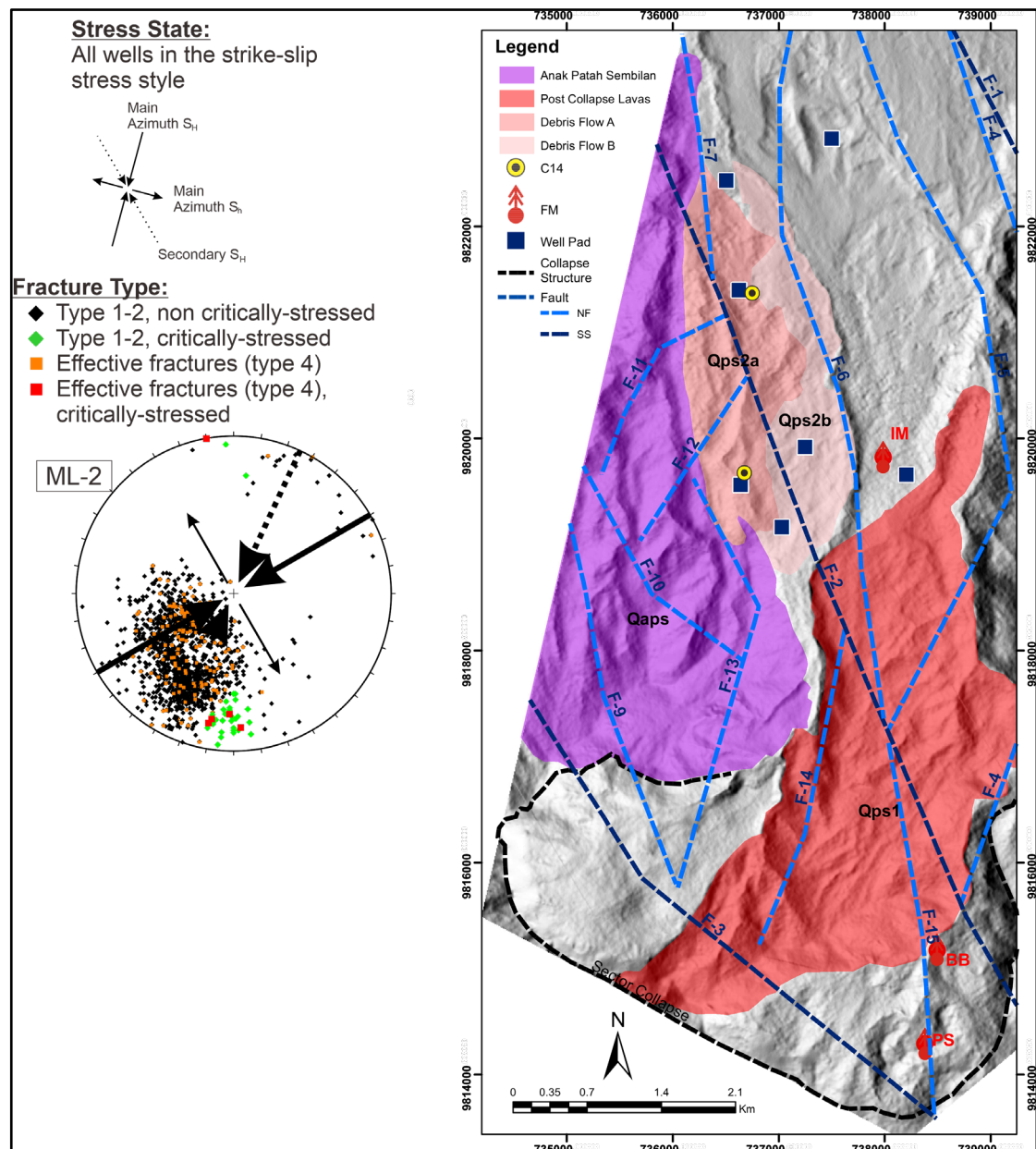
Figure 13. Detailed geologic map (from Stimac, et al., 2019), surface structure (from Supreme Energy Muara Laboh Subsurface Team, 2021), well pad locations, and stereonets show plots of poles to the fracture types. Primary and secondary maximum horizontal stress and minimum horizontal directions are also indicated.

Critically-Stressed Fractures and Well Performance

Figure 14 shows a compilation of wireline logs, informal lithology unit, feed zone intervals, and fracture profiles concerning in-situ stress. Critical fractures, represented by the green dot and having shear stress to normal stress ratio more than 0.6, are commonly present, in some situations, closely associated with feed zone intervals. The existence of a significant number of critical fractures may be connected with permeable intervals because critically-stressed fractures are hydro geologically conductive. This is exemplified by the feed zone at depth of about 2000 mMD which has a high fracture intensity of types 1+2 and a rather high critical fracture intensity. Critically-stressed of effective fractures (type 4) present in small numbers at depths of about 2000 and 2800 mMD, but show a high correlation with feed zone intervals. Around 2700-2800 mMD, in addition to the presence of critically-stressed of effective fractures (type 4), the feed zone may also be correlated with intrusion contact as

proven by the abrupt changes of gamma-ray (GR) logs pattern. Even though the feed zones have high permeability, they only have low critical fracture intensity, which can be due to permeability other than fracture, in this case, the intrusion contact with the wall rock is proven through different resistivity reflection patterns from the image log (Baroek et al., 2018). Both intrusion contact and critically-stressed fractures (type 1, 2, and 4) play important roles in the subsurface permeability pattern in the SW area of Muara Laboh field.
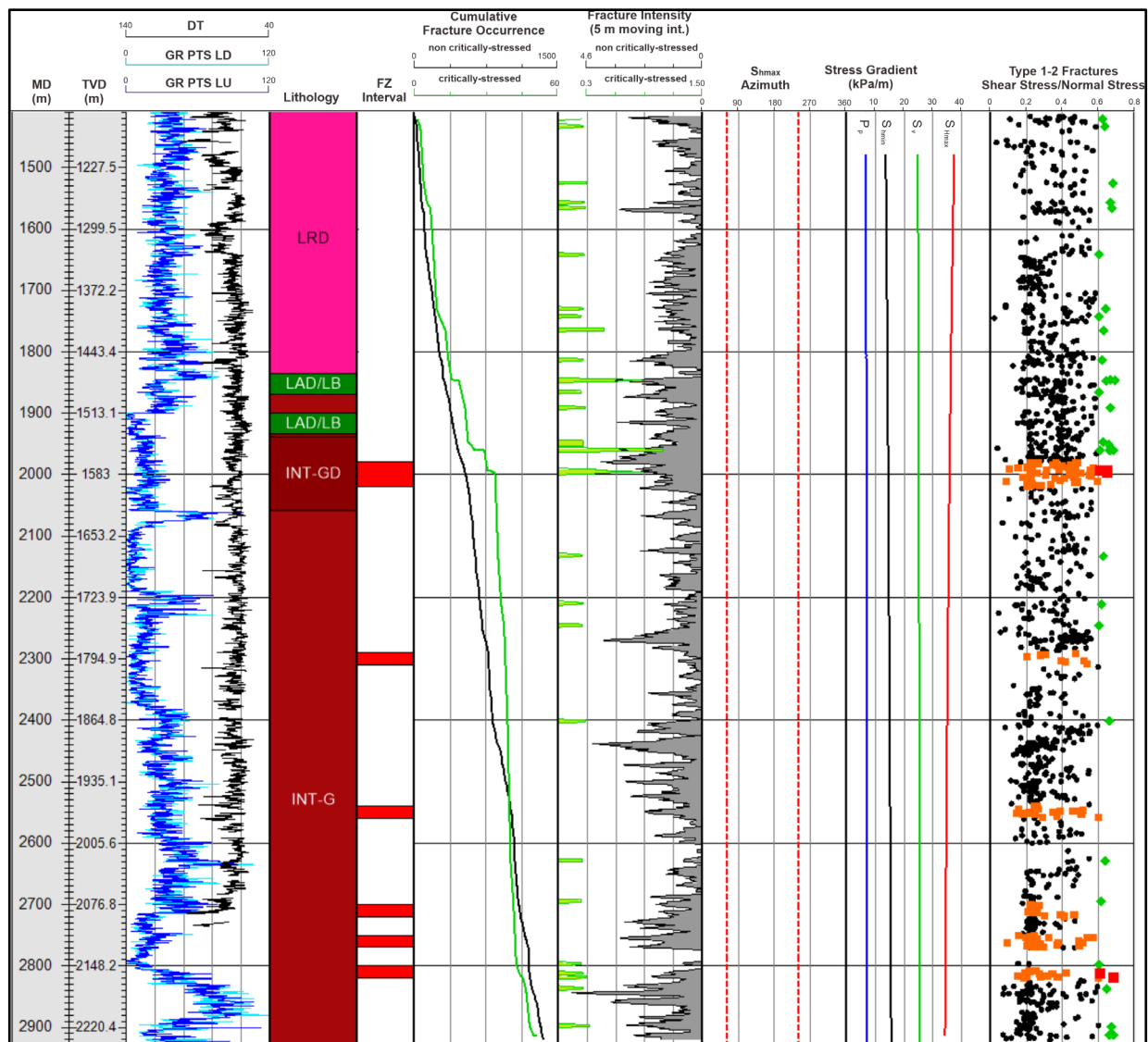

Figure 14. ML-2 data compilation, fracture and stress characterization, and geomechanical analysis.

5. CONCLUSION

Muara Laboh area is located in a pull-apart basin of the Great Sumatera Fault (GSF) due to the right stepping of the Siulak Fault segment in the north and the Suliti Fault segment in the south, resulting in several structural trend domains of NW-SE, N-S, NE-SW structures. From the observed well data, ML-2 well shows present-day in-situ stress setting is a strike-slip stress regime with maximum horizontal stress azimuth about N60°E which is consistent with the regional far-field stress in West-Central Sumatra. Critically stressed fractures appear on the fractures striking domain of NNE-SSW and E-W with vetical dips. High intensity of critically-stressed fractures ($\mu \geq 0.6$), type 1+2, and type 4 fractures tend to be associated with permeable intervals, even in a deeper feed zone, permeability is also supported by the intrusion contact with the wall rock.

ACKNOWLEDGMENT

REFERENCE

Attewell, P. B., and Farmer, I. W. (1976): *Principles of Engineering Geology*, London: Chapman and Hall.

Baroek, M. C., Stimac, J., Sihotang, A. M., Putra, A. P., and Martikno, R. (2018): Formation and fracture characterization of the Muara Laboh geothermal system, Sumatera, Indonesia, *Transactions - Geothermal Resources Council*, **42**, 1289–1315.

Barton, C. A., Castillo, D. A., Moos, D., Peska, P., and Zoback, M. D. (1998): Characterising the full stress tensor based on observations of drilling-induced wellbore failures in vertical and inclined boreholes leading to improved wellbore stability and permeability prediction, *The APPEA Journal*, **38**(1), 466–487.

Byerlee, J. (1978): Friction of rocks, *Pure and Applied Geophysics PAGEOPH*, **116**(4–5), 615–626.

Dziewonski, A. M., T.-A. Chou and J. H. Woodhouse. (1981): Determination of earthquake source parameters from waveform data for studies of global and regional seismicity, *J. Geophys. Res.*, **86**, 2825-2852.

Ekström, G., M. Nettles, and A. M. Dziewonski. (2012): The global CMT project 2004-2010: Centroid-moment tensors for 13,017 earthquakes, *Phys. Earth Planet. Inter.,* 200-201, 1-9.

Fjær, E., Holt, R. M., Horsrud, P., Raaen, A. M., and Risnes, R. (2008): *Petroleum Related Rock Mechanics* (2nd ed.), Elsevier Science, 9, 188–194.

Heidbach, O., M. Rajabi, X. Cui, K. Fuchs, B. Müller, J. Reinecker, K. Reiter, M. Tingay, F. Wenzel, F. Xie, M. O. Ziegler, M.-L. Zoback, and M. D. Zoback (2018): The World Stress Map database release 2016: Crustal stress pattern across scales, *Tectonophysics*, **744**, 484-498.

Heidbach, Oliver; Rajabi, Mojtaba; Reiter, Karsten; Ziegler, Moritz; WSM Team (2016): World Stress Map Database Release 2016, *GFZ Data Services.*

Hennings, P., Allwardt, P., Paul, P., Zahm, C., Reid, R., Alley, H., Kirschner, R., Lee, B., and Hough, E. (2012): Relationship between fractures, fault zones, stress, and reservoir productivity in the Suban gas field, Sumatra, Indonesia, *AAPG Bulletin,* **96**(4), 753–772.

Higgins, S., Goodwin, S., Donald, A., Bratton, T., and Tracy, G. (2008). Anisotropic Stress Models Improve Completion Design in Baxter Shale, *Paper SPE-115736 presented at the SPE Annual Technical Conference and Exhibition, Denver, Colorado, USA*, 21-24 September.

Jaeger, C. (1979): *Rock mechanics and engineering*, Cambridge University Press, 463.

Lockner, D. A. (1995): Rock failure, 127–147.

Matthews, W. R. and Kelly, J. (1967): How to predict formation pressure and fracture gradient, *Oil and Gas Journal*, February, 92–106.

Muraoka, H., Takahashi, M., Sundhoro, H., Dwipa, S., Soeda, Y., Momita, M., and Shimad, K. (2010): Geothermal systems constrained by the Sumatran fault and its pull-apart basins in Sumatra, Western Indonesia, *World Geotermal Congress 2010*, Bali, Indonesia, 25–29.

Mussofan, W., Baroek, M. C., Stimac, J., Sidik, R. P., Ramadhan, I., and Santana, S. (2018): Geothermal resource exploration along Great Sumatera Fault segments in Muara Laboh : Perspectives from geology and structural play, *43rd Workshop on*

Geothermal Reservoir Engineering, (2010), 1–11.

Perras, M. A. and Diederichs, M. S. (2014): A review of the tensile strength of rock: concepts and testing, *Springer International Publishing,* Switzerland.

Peska, P., and Zoback, M. D. (1995): Compressive and tensile failure of inclined well bores and determination of in situ stress and rock strength, *Journal of Geophysical Research*, **100**(B7).

Richard, P., Stephen, E., Gary, P., Donald, L., and Brian, S. (2007): The mechanical earth model concept and its application to high-risk well construction projects.

Stimac, J., Ganefianto, N., Baroek, M. C., Sihotang, M., Ramadhan, I., Mussofan, W., Sidik, R., Alfiady, Dyaksa, D. A., Azis, H., Putra, A. P., Martikno, R., Irsamukhti, R., Santana, S., Matsuda, K., Hatanaka, H., Soeda, Y., Cariou, L., and Egermann, P. (2019): An overview of the Muara Laboh geothermal system, Sumatra, *Geothermics*, **82**(January), 150–167.

Stimac, J., Sihotang, A. M., Mussofan, W., Baroek, M. C., Jones, C., Moore, J. N., and Schmitt, A. K. (2019): Geologic controls on the Muara Laboh geothermal system, Sumatra, Indonesia, *Geothermics*, **82**(May), 97–120.

Supreme Energy Muara Laboh (SEML) Subsurface Team (2021): Muara Laboh Reservoir Monitoring and Static Model Update 2021: Muara Laboh Geological Structure Update, *Unpublished manuscript*.

Tingay, M., Morley, C., King, R., Hillis, R., Coblentz, D., and Hall, R. (2010): Present-day stress field of Southeast Asia, *Tectonophysics*, **482**(1–4), 92–104.

Weingarten, J. S., and Perkins, T. K. (1995). Prediction of sand production in gas wells: methods and Gulf of Mexico case studies. *Journal of Petroleum Technology*, **47**(07), 596-600.

Wiprut, D. (2001): *Stress, boreholes stability, and hydrocarbon leakage in the Northern North Sea*, Doctoral Program Dissertation, Stanford University, 23 – 25.

Wyllie, M.R.J., Gregory, A.R. and Gardner, G. H. F. (1958): An experimental investigation of factors affecting elastic wave velocities in porous media, *Geophysics*, **23**, 459-493.

Zoback, M. D. (2007): *Reservoir geomechanics*, Cambridge University Press.

Zoback, M. D., Barton, C. A., Brudy, M., Castillo, D. A., Finkbeiner, T., Grollimund, B. R., Moos, D. B., Peska, P., Ward, C. D., and Wiprut, D. J. (2003): Determination of stress orientation and magnitude in deep wells, *International Journal of Rock Mechanics and Mining Sciences*, **40**(7–8), 1049–1076.

Zoback, M. D., and Healy, J. H. (1992): In situ stress measurements to 3.5 km depth in the Cajon Pass scientific research borehole: implications for the mechanics of crustal faulting, *Journal of Geophysical Research*, **97**(B4), 5039–5057.

Zoback, M. D., Moos, D., Mastin, L., and Anderson, R. N. (1985): Well bore breakouts and in situ stress, *Journal of Geophysical Research*, **90**(B7), 5523–5530.

Source from web site:

Global Centroid Moment Tensor (CMT) Catalog Search, retrieved from web site: https://www.globalcmt.org/ CMTsearch.html. Accessed 1 December 2021.

CASMO - Create A Stress Map Online, retrieved from web site: http://www.world-stress-map.org/casmo/. Accessed 1 November 2021.